UC San Diego
UC San Diego Previously Published Works

Title

Spatially dependent H-bond dynamics at interfaces of water/biomimetic self-assembled lattice materials

Permalink

Journal

ISSN

Authors

Wang, Haoyuan
Wagner, Jackson C
Chen, Wenfan
et al.

Publication Date

DOI

Peer reviewed

Spatially dependent H-bond dynamics at interfaces of water/biomimetic self-assembled lattice materials

Haoyuan Wang[a], Jackson C. Wagner[a], Wenfan Chen[b], Chenglai Wang[b], and Wei Xiong[a,b,1]

[a]Department of Chemistry and Biochemistry, University of California San Diego, La Jolla, CA 92093; and [b]Materials Science and Engineering Program, University of California San Diego, La Jolla, CA 92093

Understanding hydrogen-bond interactions in self-assembled lattice materials is crucial for preparing such materials, but the role of hydrogen bonds (H bonds) remains unclear. To gain insight into H-bond interactions at the materials' intrinsic spatial scale, we investigated ultrafast H-bond dynamics between water and biomimetic self-assembled lattice materials (composed of sodium dodecyl sulfate and β-cyclodextrin) in a spatially resolved manner. To accomplish this, we developed an infrared pump, vibrational sum-frequency generation (VSFG) probe hyperspectral microscope. With this hyperspectral imaging method, we were able to observe that the primary and secondary OH groups of β-cyclodextrin exhibit markedly different dynamics, suggesting distinct H-bond environments, despite being separated by only a few angstroms. We also observed another ultrafast dynamic reflecting a weakening and restoring of H bonds between bound water and the secondary OH of β-cyclodextrin, which exhibited spatial uniformity within self-assembled domains, but heterogeneity between domains. The restoration dynamics further suggest heterogeneous hydration among the self-assembly domains. The ultrafast nature and meso- and microscopic ordering of H-bond dynamics could contribute to the flexibility and crystallinity of the material—two critically important factors for crystalline lattice self-assemblies—shedding light on engineering intermolecular interactions for self-assembled lattice materials.

vibrational sum-frequency generation | lattice self-assembly | hydrogen bond | hyperspectral imaging | ultrafast dynamics

Hydrogen bond (H-bond) interaction is one of the key forces in self-assembled soft materials, which is a main avenue of research in synthetic biology (1–4). This field, known as biomimetics, seeks to create artificial organisms and includes two types of self-assemblies (5, 6). The first, comprised of soft, fluidic membrane-like lipid assemblies, has been well studied (7–9), whereas the second, rigid, crystalline lattice self-assemblies to mimic proteins, has not been investigated extensively using synthetic or nonpeptide molecules (1, 10, 11). This delayed development is because delicate H-bond interaction is necessary to balance electrostatic interactions, which play critical roles in making synthetic lattice self-assemblies resemble not only the morphology but also the behavior of their biological analog in terms of flexibility, crystallinity, and chemical functionality. Recent reports discussed lattice self-assemblies formed from sodium dodecyl sulfate (SDS) and β-cyclodextrin (β-CD), referred to hereafter as SDS@2β-CD, and showed that they satisfied the criteria to mimic protein lattice self-assemblies (5, 12, 13). The authors proposed H bonding as a key component of the strong, directional in-plane attraction force involved in maintaining two-dimensional (2D) crystallinity (12). Other works also demonstrated the influence of H bond on self-healing, proton transfer, and hydration of biomimetic materials (14–17). For example, H-bonded water was reported to influence morphology (18) and adopt the symmetry of the self-assembly (19). To determine the principles for better lattice self-assembly design, we focus on understanding the H-bond dynamics between water and self-assembled materials.

The proposed role of H bond in SDS@2β-CD is in line with the strong H-bond interactions existing between water and host

molecules in many materials and biological systems, which are critical in determining structures, dynamics, and functions of the hosts and the hydration layers (20–22). For example, pioneering work on the water dynamics of reversed micelles performed by the Fayer, Skinner, Thompson, and Pschenichnikov groups have shown that water H-bonding network dynamics are highly dependent on the size of the reversed micelles, where the dynamics of water near the surfactants are significantly reduced due to water–surfactant interactions (20–22). Petersen and coworkers also demonstrated that strong binding interactions allow water to adopt the local chirality of DNA (23). Similar templating phenomena have been observed by Perets and Yan in peptides (24).

Although H bonds have been studied in the systems mentioned above, H-bond interactions in the SDS@2β-CD system are exciting in their own right, because they are critical to the unique features of the lattice self-assembled systems (25). First, H bonds and electrostatic repulsion are the only driving forces behind these self-assemblies composed of nonamphiphilic building blocks (12). Second, these interactions allow the organic components to self-assemble into a variety of morphologies, each of which possesses a biological analog with different levels of crystallinity, making it an ideal model system for synthetic biology applications (5).

Despite its importance, H bonding in the SDS@2β-CD self-assembly remains understudied. Based on the known structure of the self-assembly (5), there are six secondary OH groups in each β-CD that cannot form H bonds directly with the OH groups of adjacent β-CDs in the same layer, due to the far distance between them. The vacant secondary OH groups are available to form H bond with water, which agrees with the thermal analysis

---

Significance

It is challenging to develop biomimetic lattice self-assemblies because such materials need to resemble the flexibility and crystallinity of their biological analog. We show that these materials exhibit unique micro- and mesoscopic-ordered ultrafast hydrogen-bond dynamics, which could be a key feature in the lattice self-assembly: the ultrafast dynamics ensure flexibility, whereas the domain-level ordering reflects crystallinity. This scientific insight cannot be revealed without the ultrafast transient vibrational sum-frequency generation microscope, which integrates ultrafast interfacial spectroscopy with interfacial molecular vibrational imaging—a state-of-the-art development.

CHEMISTRY

that indicates, on average, 4.5–7 water molecules form strong H bonds with one β-CD (Fig. 1 and *SI Appendix*, section S1), and is in line with previous studies (26–30). Furthermore, our previous vibrational sum-frequency generation (VSFG) study (19), X-ray diffraction (XRD), and atomic force microscopy-IR spectroscopy (AFM-IR) results (*SI Appendix*, section S3) suggest that there could be heterogeneity in the strongly bound water distribution of the self-assembly. Thus, the existing knowledge of strongly bound water in SDS@2β-CD begs further investigation to answer critical open questions, including, what proof is there of the H-bond interactions between β-CD and water molecules? What is the difference between the H-bond dynamics of water in the self-assemblies and that of pure water, and how are strongly bound water molecules distributed in each self-assembly?

To answer these questions, we investigate H-bond interactions and dynamics at the water/self-assembly interfaces at the individual domain level (~1 μm) by developing a spatially resolved IR pump VSFG probe microscope, which combines state-of-the-art VSFG microscopy (31–37) with pump–probe VSFG spectroscopy (38–43). We find that relaxation dynamics are different between primary and secondary OHs of β-CD, which indicates distinct H-bond environments of these OHs despite their angstrom-scale proximity. Furthermore, we observe H-bond dynamics between strongly bound water molecules and secondary OHs of β-CD, which follows a four-level-model dynamic. The relaxation dynamics of weakened water H bond show characteristics of Förster energy transfer (44). These dynamics of various domains range from 410 to 960 fs, which are longer than their counterparts of bulk water (<100 fs) (45, 46). Based on Förster energy transfer mechanism, we estimate the number of strongly bound water molecules per β-CD, thereby calculating the local hydration level in each domain. The local hydration levels in self-assembly sheets are different between domains but uniform within domains. Such a

detailed understanding of the H-bonded water and its dynamics in this system opens doors for future materials engineering and applications of biomimetic self-assemblies.

Results

The IR pump VSFG probe microscope was developed based on our previous work on a VSFG microscope (19, 47). The detailed experimental methods can be found in *Methods* and are highlighted in Fig. 2. To put the current research into context, we briefly introduce the VSFG microscope results on SDS@2β-CD (Fig. 3). In both our previous studies and this work, we focused on water/SDS@2β-CD interfaces of individual self-assembled micrometer sheets, a larger version (same morphology, e.g., crystal angles) of the nanosheet building blocks of high-order self-assembled materials (5). Thus, it represents the most basic understanding of H-bond interactions in these systems.

These self-assembled materials are chiral and noncentrosymmetric and, therefore, have strong resonant VSFG signals (19, 48–51). Plating the self-assembled sheets onto a gold substrate, we scanned the microscope to measure the VSFG spectra of each spatial point. A representative VSFG intensity-mapped image of the sample is shown in Fig. 3*A*, where bright spots represent self-assembled sheet domains. Each pixel in the image encodes a VSFG spectrum, and all spectra were fitted with Voigt profiles. Based on the fitting results (a representative spectrum from domain E is shown in Fig. 3*B*), we observed three CH peaks and three OH peaks. We only focused on the OH peaks in this work since they are sensitive to H bonds. Based on dehydration and H_2O/D_2O exchange experiments, we assigned the three OH peaks to strongly bound water (~3,050 cm^{-1}), secondary OHs of β-CD (~3,280 cm^{-1}), and primary OHs of β-CD (~3,350 cm^{-1}) (Fig. 3*B*) (19). We noted that the peaks at ~3,050 cm^{-1} and ~3,280 cm^{-1} also had contributions from secondary OHs and
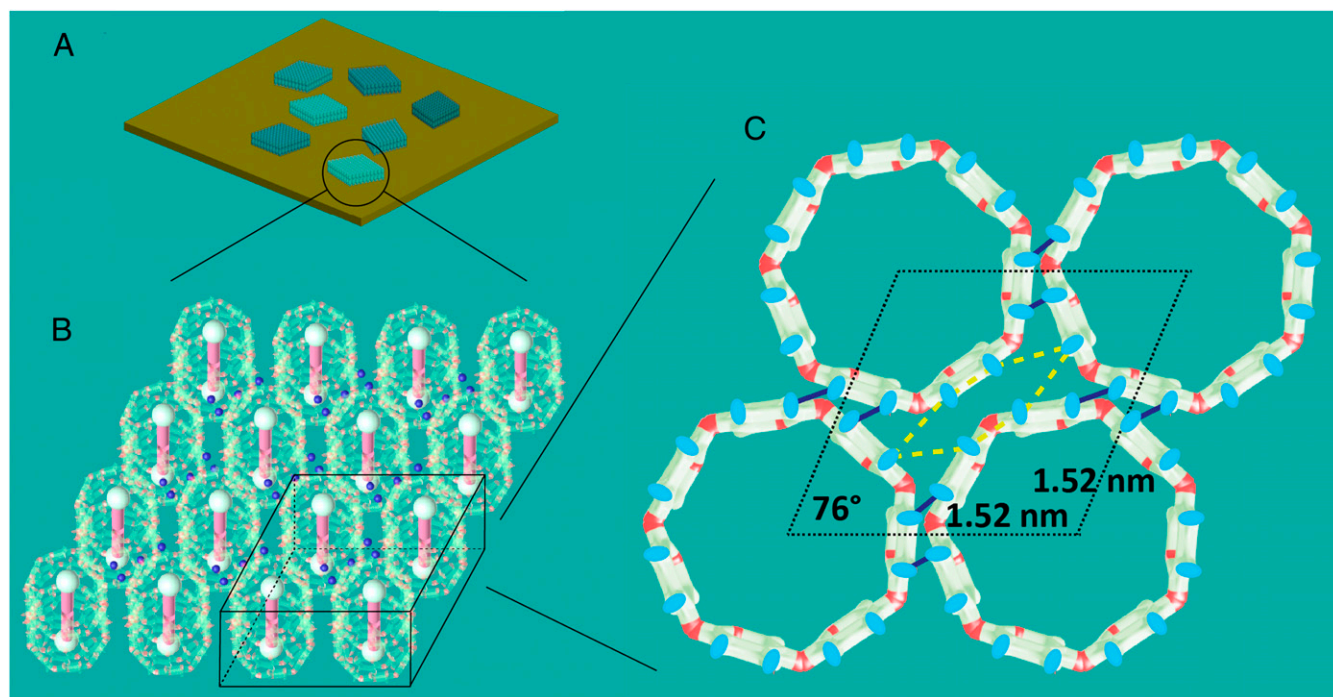

Fig. 1. (*A*) Schematic of the SDS@2β-CD self-assembly sheets with different hydration levels (represented by different blue color depth) on a gold slide. (*B*) A zoomed view of one sheet in *A* from a tilted angle. Blue dots represent strongly bound water. The variation of the number of water molecules reflects the potential heterogeneity of the strongly bound water numbers in each site. Only one layer of strongly bound water is shown for better visualization. (*C*) Top view of one SDS@2β-CD unit shown in the box of *B*. The secondary OH of β-CD is shown as cyan shapes. Dark-blue lines that connect the secondary OHs are H bonds between secondary OHs. The yellow dashed lines label the cavity formed by the secondary OHs that are available to form H bonds with water (details in *SI Appendix*, section S1). The crystal parameters in *C* are from ref. 5.
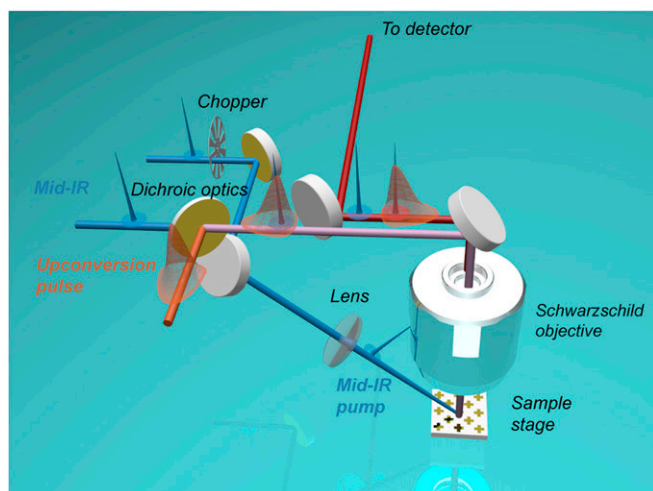
Fig. 2. Schematic of the spatially resolved IR pump VSFG probe microscope. Mid-IR and upconversion pulses are combined collinearly and overlapped temporally by a customized dichroic optic. These incident beams are focused on the sample through a Schwarzschild objective lens. The pump mid-IR pulse is focused onto the sample using a focal length f = 10-cm calcium fluoride lens with an incident angle of ~60° from a different arm. To compensate for shot-to-shot fluctuation, we implemented a quasi–shot-to-shot detection scheme: a chopper is used to block every other pump pulse, and a Galvo mirror redirects VSFG signals with and without pump pulse onto different rows of the CCD detector.

strongly bound water OH, respectively, due to hybridization between these two modes (19, 23, 24). The existence of a water VSFG signal was because of the strong interactions between water and the secondary OH groups of β-CD, making water adopt the symmetry of the materials and, therefore, became VSFG active (19, 24). Under the same experimental conditions, VSFG signals from air/water interfaces were negligible. Thus, despite probing a nonplanar surface, VSFG still revealed water structures at the water/SDS@2β-CD interfaces.

By comparing the VSFG spectra of OH groups of individual domains (Fig. 3C), we can learn the hydration level of these domains. Fig. 3C shows that the spectra in some domains have more prominent secondary OH peaks than others. Previously (19), we concluded that the secondary to primary OH peak intensity ratio had a monotonic relationship with relative humidity (RH) of the environments in the range of 25–40% of RH. A further study of deuterated SDS@2β-CD (*SI Appendix*, section S2) indicates this relationship becomes nonmonotonic when the RH is above 40%. Thus, although the variation in OH peak intensities reveals heterogeneity in local hydration levels between each domain (in agreement with the XRD and AFM-IR data, *SI Appendix*, section S3), it cannot quantitatively reveal the local hydration level. The question of how local strongly bound water influences H-bond dynamics at interfaces of individual self-assembled sheets motivates the present study.

Dynamics of OHs of β-CD. When water is strongly bounded to self-assembled materials, there are two possible changes to water dynamics. First, the templated water network H-bond dynamics could be different from bulk water, which is known to have fast energy dissipation (52). Second, heterogeneity in the self-assembly host materials could ultimately lead to spatial heterogeneity in H-bond dynamics at water/SDS@2β-CD interfaces. To examine whether such changes exist, we perform spatially resolved ultrafast measurements.

When excited by IR pulses, three distinct transient features are observed in the OH spectral regime. As shown in Fig. 4, the

two higher-frequency features are related to OHs of β-CD, which we will discuss first. In Fig. 4 *A* and *C*, we plot the two most representative pump–probe dynamics of the OH spectral features (from domains A and E of Fig. 3*A*), with the dynamics of the remaining domains in Fig. 3*A* summarized in *SI Appendix*, section S4. The primary OH peak is bleached, shown as negative dynamics at 3,350 cm^{-1} in Fig. 4 *A* and *C*, and it lasts longer than 1.8 ps—the longest time delay scanned. The negative bleach dynamic is caused by removing the primary OH population from the ground vibrational states. Since the bleach dynamics for the primary OH of all domains exhibit long lifetimes (*SI Appendix*, section S4), it indicates that the primary OH for all sheets experiences similar isolated or weak/no H-bond environments, leading to slow energy relaxation (53).

Secondly, in some spots, the secondary OH peak near 3,280 cm^{-1} also has a short-lived bleach dynamic (Fig. 4*C*) with a lifetime of 280–400 fs. The fast decay dynamics suggest that secondary OH can quickly dissipate its energy into the environment, agreeing with its H-bonded nature. However, the intensity and existence of the secondary OH dynamics vary significantly from spot to spot (see Fig. 4*A* and *SI Appendix*, section S4). This variation is likely correlated to the intensities of the secondary OH static VSFG peak. For example, domains A/B/C/K do not have the bleached secondary OH dynamics, and in the static VSFG spectra, the secondary OH signals in these domains are small as well.

The drastically different dynamics of primary and secondary OHs indicate distinct local environments. Comparing to the secondary OHs, the primary OHs are at the narrower rim of β-CDs, and therefore the distances between primary OHs from adjacent β-CDs are much larger. This distance difference could make the formation of primary OHs-water bridges less likely. Also, assuming their distance is approximately the depth of β-CD, then the primary and secondary OHs are separated by about 0.8 nm, which
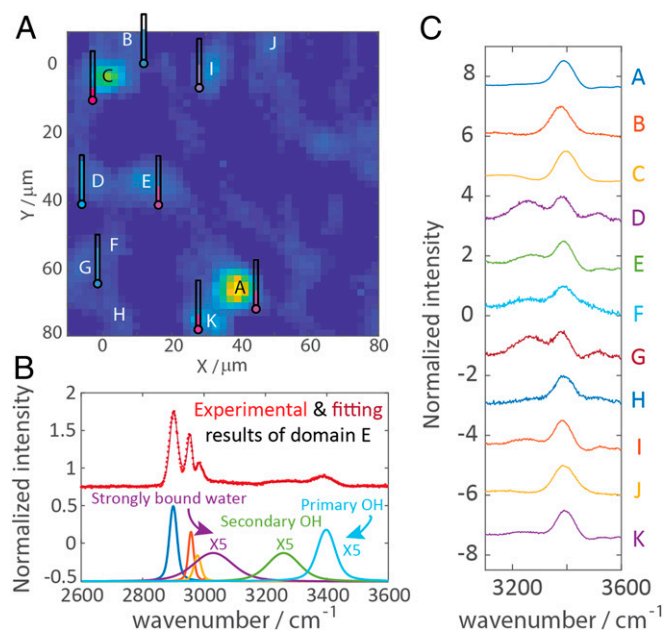

Fig. 3. (*A*) VSFG intensity image (PPP polarization) for the OH region of molecular self-assembled micrometer sheets. The hygrometer next to each domain represents the relative hydration level determined in Table 1. (*B*) A representative VSFG spectrum from domain E and its spectral fitting reveals that there are three CH peaks and three OH peaks, which correspond to strongly bound water, secondary and primary OH from β-cyclodextrin, respectively. (*C*) Individual zoomed-in spectra for OH region. All spectra have been normalized to their maximum and have been offset vertically for better visualization.
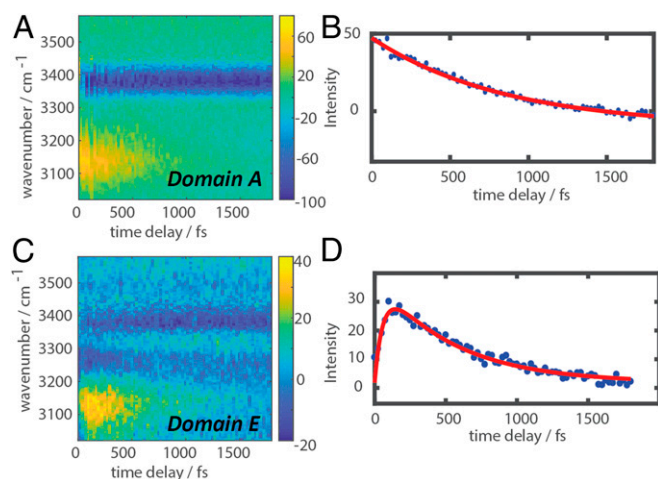
Fig. 4. Two representative types of vibrational dynamics. (*A*) Domain A has long-lasting bleach dynamics for primary OH from β-cyclodextrin and has a positive signal for water OH, which shows a monotonical decay (as shown in *B*). (*C*) Domain E has long-lasting bleach dynamics for primary OH from β-cyclodextrin, a short-lived bleach dynamic for secondary OH from β-cyclodextrin, and a positive signal for water OH in a delayed fashion (as shown in *D*). *B* and *D* are the integrated signal for the strongly bound water OH frequency region near 3,150 cm^{-1}.

highlights the proximity of this ordering. This contrast suggests that upon self-assembling, the H-bond network is so ordered that water is templated precisely near secondary OHs of β-CDs. Thus, despite the proximity of the two OH groups, they could have very different local environments, which, from a biochemical perspective, could enhance proton transfer and be necessary for functions of natural and artificial biological systems and influence membrane dipole potentials (44).

Dynamics of H-Bond Weakening and Restoration. Finally, we focus on the positive transient peak at ~3,150 cm^{-1}, which is associated with the OH feature of strongly bound water. There are two interesting features worth noting about this dynamic. First, the dynamic signal is positive, and, second, the peak center blueshifts from ~3,050 cm^{-1} (obtained from static VSFG measurements) to ~3,150 cm^{-1}. The nature of the positive peak is realized by a narrow-band IR pump VSFG probe, using IR filters to pump different OH modes selectively. By selectively pumping the primary

OH mode (filter 3), no pump–probe dynamics are observed while, when all modes except the primary OH are pumped (filter 1), similar dynamics are observed near ~3,150 cm^{-1}. These results conclude that the positive dynamics are not related to the primary OH. In addition, when all modes except the primary and secondary OH are pumped (filter 2), a small positive dynamic is observed. These experiments, summarized in Fig. 5, indicate that the positive dynamics can be attributed to the excitation of the secondary OH, while similar but weaker intensity dynamics are observed when pumping strongly bound water. (The possibility of overtone peaks of secondary OH and interferences are also examined and excluded [*SI Appendix*, sections S11 and S12].)

Since the positive dynamic peak at ~3,150 cm^{-1} is blueshifted relative to the strongly bound water OH peak at ~3,050 cm^{-1}, we can assign it to a weakening of the H bond between water and the secondary OH of SDS@2β-CD. This assignment agrees with the fact that both peaks have mixed origins from water and the secondary OH. Therefore, when either or both modes are pumped, H-bond weakening is observed. We note the blueshift should also generate a transient negative signal appearing at 3,050 cm^{-1}, which is very small due to the pseudoheterodyne detection (*SI Appendix*, section S7).

We performed a spatially resolved transient VSFG experiment on deuterated SDS@2β-CD to further understand the mechanism behind the positive dynamics seen at ~3,150 cm^{-1}. The results (Fig. 6) agree with the OH dynamics (Fig. 4). The transient features of the deuterated samples match well with the nondeuterated sample, with the negative peak at ~2,540 cm^{-1} corresponding to the primary OH of SDS@2β-CD, which has a long lifetime, and the positive peak at ~2,400 cm^{-1} corresponding to the weakening/restoration of the H bond, which shows a relatively short-lived dynamic. Only domain OD1 has a short-lived bleach dynamic of secondary OH—consistent with the observation for the nondeuterated samples.

A quantitative comparison between the deuterated and nondeuterated system can help elucidate the nature of the H-bond weakening and recovery dynamics. All positive H-bond dynamics measured at different spatial domains are fitted and are summarized in Table 1 (see *SI Appendix*, sections S4 and S6 for full lifetimes). Statistically, we find that deuteration does not affect the weakening dynamics significantly (rising dynamics, t$_1$), while deuteration drastically slows the relaxation dynamics. In the H-bond dynamics of water systems, fast dynamics within 150 fs are attributed to H-bond fluctuations through hindered translation motions, e.g., increase of O–O bond distance (54–57). The fact that the
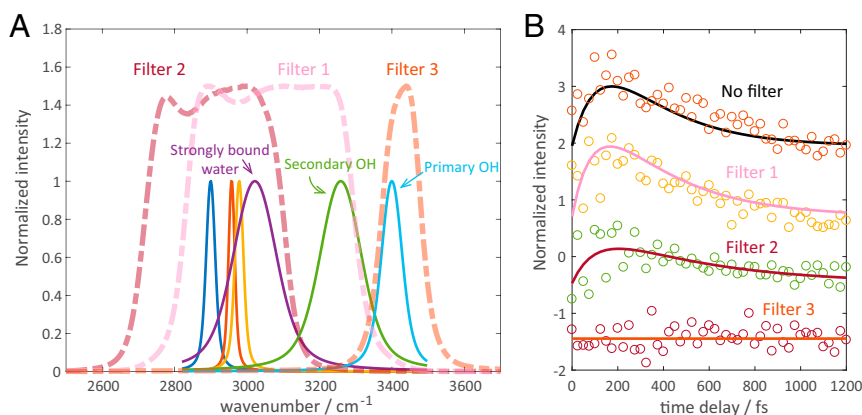

Fig. 5. (*A*) Spectral coverage of the three filters in the narrow-band pump VSFG probe experiment. (*B*) Dynamic traces of the strongly bound water peak with different selective filters from the same spatial point. The pump power intensity variation is considered, and all of the dynamics' intensities are normalized to the one without any filter. Filter 1 dynamics are nearly the same as the dynamics without any filter, while filter 3 does not show any signal. Filter 2 shows a weak positive dynamic.
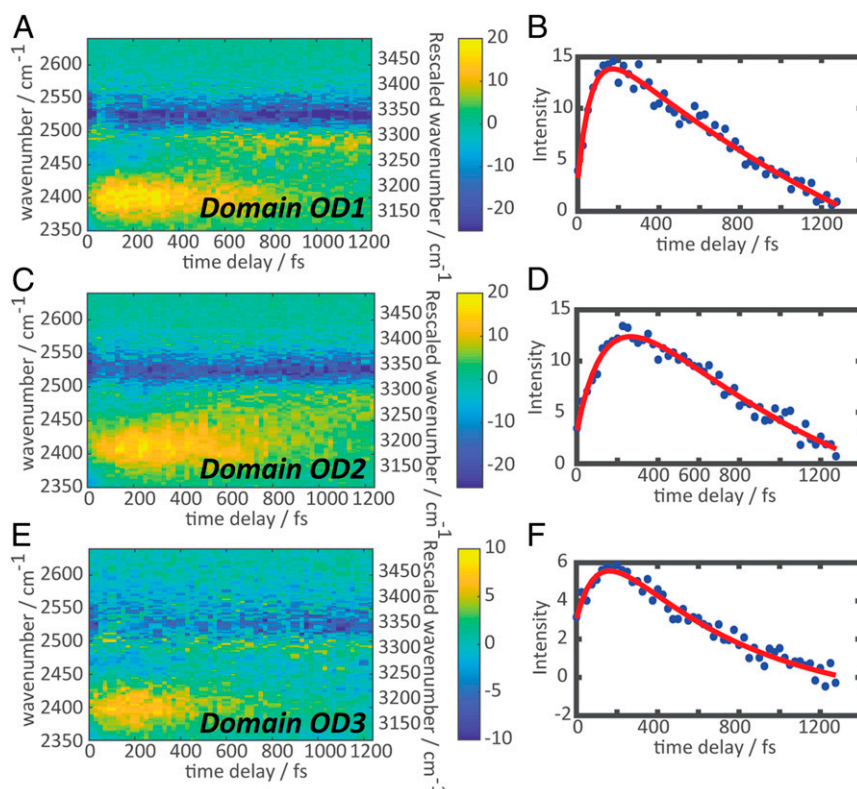
Fig. 6. (*A*, *C*, and *E*) Dynamics traces from the deuterated SDS@2β-CD sample in the OD region. *y* axis on the right is the rescaled frequency using a ratio of 0.755, slightly different from the ratio in the gas phase (0.742) due to anharmonicity. (*B*, *D*, and *F*) Integrated positive dynamics signal from the corresponding dynamics trace.

H-bond weakening dynamic seen here is insensitive to deuteration implies that a similar O–O bond elongation mechanism could be responsible for the H-bond weakening.

In contrast, deuteration slows the relaxation dynamics by about twice. Such an effect suggests that the relaxation involves Förster energy transfer, which exists in water systems where OH modes of water are closely overlapped (45, 58). In the literature, the energy transfer rate was also determined to be about 2.3 times more efficient for the OH band than the OD band due to the difference in transition dipole moments (59), which agrees with our experimental observation. Contributions from other dynamics, i.e., wobbling-in-a-cone and energy transfer to CH modes, are considered and excluded (see *SI Appendix*, sections S8 and S10 for details).

Combining all experimental observations, we adopt the existing four-level model (41) developed for ultrafast water vibrational dynamics to describe the H-bond vibrational dynamics at water/SDS@2β-CD interfaces (Fig. 7): The IR pulse first excites the secondary OH of β-CD or OH groups of strongly bound water. OH then transfers its energy to the surrounding H-bond network, resulting in a H-bond elongation coupled with a reduction in bond strength. The weakened H bond is restored to its original strength by transferring additional energy to its surroundings through Förster resonant energy transfer processes. We further simulate the spectral dynamics based on the four-level model (*SI Appendix*, section S7). The simulated dynamics of the positive signal at ~2,400 cm^{-1} (*SI Appendix*, Fig. S11) match well with experimental results, validating the four-level model to describe the H-bond dynamics in this system.

Despite the fact that H-bond dynamics manifest as 2D spectral dynamics, we find the 1D dynamic traces at ~2,400 cm^{-1} in Fig. 6 (and ~3,150 cm^{-1} for OH in Fig. 4) can still accurately capture the actual H-bond dynamics. We confirm this by fitting the

dynamics at ~2,400 cm^{-1} of a set of 2D spectral dynamics, which are modeled by biexponentials, in which t_1 and t_2 describe the initial weakening and relaxation process, respectively, in the four-level model (see *SI Appendix*, section S7 for details). We find that despite the fitted t_1 and t_2 and the original t_1 and t_2 being different, they form a one-to-one relationship. Therefore the dynamics at ~2,400 cm^{-1} are a decent descriptor of the H-bond dynamics. The relationship is summarized as *SI Appendix*, Table S2 and is used to extract the original H-bond dynamics from the apparent dynamics. The H-bond relaxation lifetime t_2 is found to

Table 1. The dynamic lifetimes fitted by a biexponential model: t_2 is H-bond relaxation lifetime, from which we calculated relative hydration level

Domain	t_1, fs	Apparent t_2, fs	Corrected t_2, fs	Relative hydration level
OH dynamics				
A	NA	832 ± 81	708 ± 45	2.64
B	NA	456 ± 25	468 ± 18	4.04
C	141 ± 31	770 ± 67	958 ± 74	2.14
D	48 ± 8	359 ± 64	410 ± 66	5.11
E	68 ± 9	594 ± 98	659 ± 92	2.76
G	40 ± 10	408 ± 69	452 ± 65	4.35
I	NA	562 ± 40	542 ± 27	3.26
K	91 ± 3	730 ± 16	827 ± 16	2.38
OD dynamics				
OD1	70 ± 4	1640 ± 530	1358 ± 291	2.94
OD2	150 ± 4	1270 ± 470	1375 ± 347	2.92
OD3	106 ± 4	690 ± 28	820 ± 29	5.67

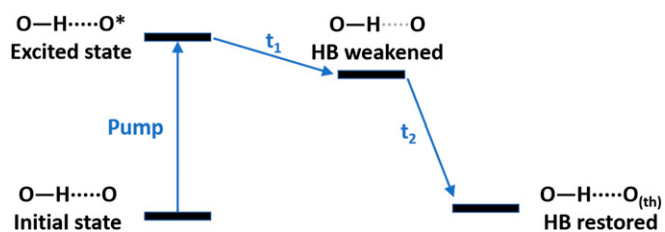See details in *SI Appendix*, section S9.

Fig. 7. The four-level model that describes the OH (OD) dynamics in self-assembly.

range from 410 to 960 fs (Table 1), which is slower than Förster energy transfer rate in bulk water (<100 fs) or ice (300 fs) (45, 46). The slower transfer efficiency of OH in the confined environment could come from the lower mode density and less spectral overlapping that occurs between water and OH of β-CD compared to that seen between waters.

Domain-dependent H-Bond Dynamics. Next, we examine the spatial heterogeneity of the H-bond dynamics at ~3,150 cm^{-1}. From Fig. 4, we present the most extreme cases found in domains A and E (Fig. 4 *A* and *B*; other results are shown in *SI Appendix*, section S4). In this extreme case, the positive peak appears immediately after excitation and decays monotonically in domain A. In domain E, however (Fig. 4 *C* and *D*), the positive peak appears in a delayed fashion. Similar spatially heterogeneous dynamics are observed in deuterated samples, as they all rise and decay at different rates (Fig. 6). We carefully quantified the measurement's uncertainty (*SI Appendix*, sections S4 and S6) and ruled out temporal artifacts (a variation of $^{+/-}$12 fs) by measuring time zero through a third-order signal (*SI Appendix*, section S13). Thus, the observed heterogeneous dynamics reflect domain-specific H-bond dynamics.

The fitting results using the biexponential function (Table 1 and *SI Appendix*, sections S4 and S6) quantify the domain-specific H-bond dynamics. For the regular (deuterated) sample, the H-bond weakening dynamics range from instantaneous to 140 fs (70–150 fs), while the relaxation dynamics range from 410 to 960 fs (820 fs to 1.4 ps). Based on the four-level model and theoretical study from Staib and Hynes, the variation of H-bond weakening dynamics suggests a variety in H-bond strength (56).

We then focus on modeling the relaxation dynamics because it is related to the amount of local strongly bound water. To do so, we build a model that correlates the relaxation dynamics with the number of strongly bound water (*SI Appendix*, section S9). The model assumes that the hydration level of individual β-CD fluctuates between 2–6 water molecules, and water is at equilibrium (lowest energy calculated from a H-bond potential), from which we calculate the OH-OH distance at different hydration levels. We further calculate the hydration-level-specific Förster energy transfer rate based on the OH-OH distances and known Förster energy radius and OH lifetime. We find that from 2 to 6 strongly bound water molecules per β-CD molecule, the relaxation lifetime spans from 1.04 ps to 330 fs, and if a domain has a mixture of a different density of strongly bound water, the measured t_2 is the geometric mean of those two limits. Based on this empirical relationship, we summarize the hydration level of each domain in Table 1 and Fig. 3*A*. The relative hydration level ranges from 2.1 to 5.7 water molecules per β-CD molecule, which suggests the actual hydration of strongly bound water per β-CD is strongly domain-specific. A possible driving force of such local hydration heterogeneity is the lattice structure variations of different domains (e.g., small variations of secondary OHs distances or the hexagonal exterior cavity angles). Such a detailed insight into local hydration of the self-assembled materials cannot be gained from static VSFG imaging measurements (60).

Another stunning contrast is that both spectra and dynamics of different areas within an individual domain are similar (*SI Appendix*, section S15). This contrast means there are similar H-bond coupling strength and hydration levels within domains. This intriguing observation implies that the mesoscopic organization of each SDS@2β-CD domain governs the H-bond interactions and strongly bound water arrangement at water/SDS@2β-CD interfaces. This observation is a mesoscopic analog of the microscopic water–host interaction observed in water–ion and water–reverse micelle clusters where water dynamics vary based on the specific water–ion pair (61) or the specific location of water in the reverse micelle (20–22).

Discussion and Conclusion

Generally, pure water and dilute aqueous solutions are essential. However, water/material interactions are equally important as they can significantly affect functions of materials and biological systems. In SDS@2β-CD, we demonstrate a unique coordinated H-bond interaction in these self-assembled systems. Mesoscopically, the H-bond network distribution appears uniform within each domain, and microscopically distinct H-bond interactions are also preserved well between two types of OHs of β-CD that are separated by angstroms. The implication that strongly bound water and related H-bond dynamics are spatially heterogeneous when bound in host systems differs from the conventional perception that water dynamics are spatially homogeneous. This conclusion could offer new insights on water's role in protein mimetic self-assemblies: the ultrafast dynamics of weakening and restoring of H bond ensures flexibility. At the same time, the ordering presented in the microscopic and mesoscopic domain represents the crystallinity of the self-assemblies. These properties are essential for controlling the structure and dynamics of stimulated-responsive materials and biomimetic lattice self-assemblies.

While the focus of this study is to understand H-bond dynamics in SDS@2β-CD, the open question of whether templated water dynamics could exist in other self-assembled materials remains unanswered. Since strong H-bond interactions exist between water and lipid or protein-based self-assemblies, such as membranes or viruses (62–64), similar phenomena likely exist. Interesting systems that could exhibit similar mesoscopic H-bond interaction heterogeneity include ice-nucleating bacterial proteins, which could provide a template for first hydration layer ordering to seed ice formation at relatively low temperatures (65). Another biological system involving ordered water uses strongly bound water as a molecular adhesive between two proteins, which is vital for cellular recognition processes (15). This strong H-bond–induced local ordering could also exist in other artificial self-assemblies, such as covalent-organic-frameworks, metal-organic-frameworks, and saccharide-based assemblies (66–68). Since these systems possess hydrophilic analogs, first hydration layer templating could be studied as well. We note that VSFG microscopy requires systems with chirality or a lack of inversion symmetry. However, all proposed systems offer a subset of analogs that possess this symmetry and, therefore, are good candidates.

More insights into local H-bond dynamics and hydrations of self-assembled systems can be obtained by further developing time-resolved VSFG microscopy. First, local spectral heterogeneity, dephasing dynamics, and spectral diffusion can be measured with a spatial resolution by developing ultrafast 2D-VSFG microscopy (43, 69–72). Second, the limit of the spatial resolution can be overcome by employing a larger numerical aperture Schwarzchild objective and adapting superresolution methods (73–76). Lastly, with the advent of multihundred kHz laser systems (77), a complete hyperspectral-dynamic molecular imaging technique based on the methods outlined here is on the horizon for studying self-assembled chiral and molecular monolayer systems (78, 79).

Methods

Experimental Setup. The core experimental setup for the pump-probe SFG microscope is illustrated in Fig. 2. A mid-IR pulse (7 μJ) is generated by a TOPAS (Light Conversion) pumped by a Ti: sapphire 30-fs, 800-nm laser with 1-kHz repetition rate (Coherent), followed by a home-built difference frequency generation set up using a KTA crystal (Eksma Optics Inc., Type II). The mid-IR pulse has a center frequency of 3,200 cm^{-1} with 500-cm^{-1} full width at half maximum (FWHM) and 70-fs pulse duration. The full mid-IR output is ∼7 μJ, and a calcium fluoride beam splitter is used to split the beam into two arms: 0.5 μJ of the mid-IR pulse is used for the VSFG probe, and the rest is used as a mid-IR pump. The polarizations of all beams are controlled individually by λ/2 waveplates and polarizers. The signal polarization is analyzed by a polarizer in front of the spectrograph. The residue of the 800-nm beam after the TOPAS passes through an etalon filter to generate the upconversion pulse (FWHM 5 cm^{-1}). The beam mode of the upconversion pulse is optimized by passing through a spatial filter. The mid-IR and upconversion pulses are first combined with a customized dichroic optic (Newport) that reflects 800-nm light and transmits mid-IR. The combined beams are then focused together onto the sample with an incident angle of about 18° by a Schwarzchild (Edmund Optics, 15×/0.28 NA) reflective objective, and the emitted signal is picked up by a gold mirror. The pump mid-IR pulse is focused onto the sample using an f = 10-cm calcium fluoride lens with an incident angle of ∼60° in a different arm. Therefore, the VSFG signal generated by the pump mid-IR and upconversion pulses has a slightly different trajectory than the probe SFG signal, and a razor blade is used to block the pump VSFG signal. A motorized stage scans the time delay between the mid-IR pump and the VSFG probe. To compensate for pulse-to-pulse fluctuation of the probe mid-IR and upconversion pulses, a chopper (Thorlabs Inc. PN MC200B) is used to block every other pump mid-IR pulse, and a Galvo mirror (Thorlabs Inc. PN GVSM001) redirects the SFG signal with and without pump pulse onto different rows of the charged-couple device (CCD) detector (*SI Appendix*, section S16). Both signals are collected using the multitrack mode.

Therefore, quasi–shot-to-shot pump–probe spectra can be obtained. The sample is rastered by a computerized stage (Mad City Labs) under the microscope, and spectra of each location are measured by a spectrograph (Andor) and the CCD (Andor) and recorded by a home-made LabVIEW code. The spatial scan step is 2 μm since the resolution is determined to be ∼1.8 μm (47).

The full dynamics are obtained by scanning relative time delays between the IR pump and VSFG probe beams. However, to generate a complete pump–probe spectral-dynamic image, a 3D scan must be taken, which takes at least a few days. Thus, to optimize the data acquisition efficiency, an adaptive approach is implemented in which full VSFG spectral images are first scanned, and then spatial pixels with strong signals and distinct line shapes are chosen for pump–probe scans.

Data Availability. Data, figure, and code data have been deposited in Zenodo (http://doi.org/10.5281/zenodo.3888869) including dynamics data for OH and OD regime, dynamics data with spectral filters, VSFG spectra at different RH conditions, AFM-IR data, XRD data, thermal gravimetric analysis (TGA) data, differential scanning calorimetry (DSC) data, and the codes to simulate water locations in *SI Appendix*.

1. K. T. Nam *et al.*, Free-floating ultrathin two-dimensional crystals from sequence-specific peptoid polymers. *Nat. Mater.* **9**, 454–460 (2010).
2. C. Valéry *et al.*, Biomimetic organization: Octapeptide self-assembly into nanotubes of viral capsid-like dimension. *Proc. Natl. Acad. Sci. U.S.A.* **100**, 10258–10262 (2003).
3. A. Aliprandi, M. Mauro, L. De Cola, Controlling and imaging biomimetic self-assembly. *Nat. Chem.* **8**, 10–15 (2016).
4. G. M. Whitesides, B. Grzybowski, Self-assembly at all scales. *Science* **295**, 2418–2421 (2002).
5. S. Yang *et al.*, Giant capsids from lattice self-assembly of cyclodextrin complexes. *Nat. Commun.* **8**, 15856 (2017).
6. C. Wu, Q. Xie, W. Xu, M. Tu, L. Jiang, Lattice self-assembly of cyclodextrin complexes and beyond. *Curr. Opin. Colloid Interface Sci.* **39**, 76–85 (2019).
7. S. Clarke, The hydrophobic effect: Formation of micelles and biological membranes, 2nd edition (Tanford, Charles). *J. Chem. Educ.* **58**, A246 (1981).
8. D. E. Discher, A. Eisenberg, Polymer vesicles. *Science* **297**, 967–973 (2002).
9. M. S. Nikolic *et al.*, Micelle and vesicle formation of amphiphilic nanoparticles. *Angew. Chem. Int. Ed. Engl.* **48**, 2752–2754 (2009).
10. M. Dubois *et al.*, Self-assembly of regular hollow icosahedra in salt-free catanionic solutions. *Nature* **411**, 672–675 (2001).
11. M. Dubois *et al.*, Shape control through molecular segregation in giant surfactant aggregates. *Proc. Natl. Acad. Sci. U.S.A.* **101**, 15082–15087 (2004).
12. L. Jiang *et al.*, "Annular Ring" microtubes formed by SDS@2β-CD complexes in aqueous solution. *Soft Matter* **6**, 1731–1736 (2010).
13. L. Jiang, Y. Peng, Y. Yan, J. Huang, Aqueous self-assembly of SDS@2β-CD complexes: Lamellae and vesicles. *Soft Matter* **7**, 1726–1731 (2011).
14. M. Wikström, M. I. Verkhovsky, G. Hummer, Water-gated mechanism of proton translocation by cytochrome c oxidase. *Biochim. Biophys. Acta* **1604**, 61–65 (2003).
15. Y. Levy, J. N. Onuchic, Water mediation in protein folding and molecular recognition. *Annu. Rev. Biophys. Biomol. Struct.* **35**, 389–415 (2006).
16. P. Cordier, F. Tournilhac, C. Soulié-Ziakovic, L. Leibler, Self-healing and thermo-reversible rubber from supramolecular assembly. *Nature* **451**, 977–980 (2008).
17. F. Liu, B. Q. Dong, X. H. Liu, Y. M. Zheng, J. Zi, Structural color change in longhorn beetles Tmesisternus isabellae. *Opt. Express* **17**, 16183–16191 (2009).
18. C. Zhou, X. Cheng, Y. Yan, J. Wang, J. Huang, Reversible transition between SDS@2β-CD microtubes and vesicles triggered by temperature. *Langmuir* **30**, 3381–3386 (2014).
19. H. Wang, W. Chen, J. C. Wagner, W. Xiong, Local ordering of lattice self-assembled SDS@2β-CD materials and adsorbed water revealed by vibrational sum frequency generation microscope. *J. Phys. Chem. B* **123**, 6212–6221 (2019).
20. S. Abel *et al.*, On the structural and dynamical properties of DOPC reverse micelles. *Langmuir* **32**, 10610–10620 (2016).
21. E. E. Fenn, D. B. Wong, C. H. Giammanco, M. D. Fayer, Dynamics of water at the interface in reverse micelles: Measurements of spectral diffusion with two-dimensional infrared vibrational echoes. *J. Phys. Chem. B* **115**, 11658–11670 (2011).
22. A. A. Bakulin *et al.*, Dynamics of water confined in reversed micelles: Multidimensional vibrational spectroscopy study. *J. Phys. Chem. B* **117**, 15545–15558 (2013).
23. M. L. McDermott, H. Vanselous, S. A. Corcelli, P. B. Petersen, DNA's chiral spine of hydration. *ACS Cent. Sci.* **3**, 708–714 (2017).
24. E. A. Perets, E. C. Y. Yan, Chiral water superstructures around antiparallel β-sheets observed by chiral vibrational sum frequency generation spectroscopy. *J. Phys. Chem. Lett.* **10**, 3395–3401 (2019).
25. W. Khuntawee, M. Karttunen, J. Wong-Ekkabut, A molecular dynamics study of conformations of beta-cyclodextrin and its eight derivatives in four different solvents. *Phys. Chem. Chem. Phys.* **19**, 24219–24229 (2017).
26. S. Makedonopoulou, I. M. Mavridis, Structure of the inclusion complex of β-cyclodextrin with 1,12-dodecanedioic acid using synchrotron radiation data; a detailed dimeric β-cyclodextrin structure. *Acta Crystallogr. B* **56**, 322–331 (2000).
27. P. Giastas, K. Yannakopoulou, I. M. Mavridis, Molecular structures of the inclusion complexes β-cyclodextrin-1,2-bis(4-aminophenyl)ethane and β-cyclodextrin-4,4'-diaminobiphenyl; packing of dimeric β-cyclodextrin inclusion complexes. *Acta Crystallogr. B* **59**, 287–299 (2003).
28. M. M. Pop *et al.*, Crystal structure of the inclusion complex of β-cyclodextrin with mefenamic acid from high-resolution synchrotron powder-diffraction data in combination with molecular-mechanics calculations. *Acta Crystallogr. B* **58**, 1036–1043 (2002).
29. T. Aree, B. Schulz, G. Reck, Crystal structures of β-cyclodextrin complexes with formic acid and acetic acid. *J. Incl. Phenom.* **47**, 39–45 (2003).
30. T. Aree, N. Chaichit, Crystal structure of β-cyclodextrin-benzoic acid inclusion complex. *Carbohydr. Res.* **338**, 439–446 (2003).
31. K. Cimatu, S. Baldelli, Sum frequency generation microscopy of microcontact-printed mixed self-assembled monolayers. *J. Phys. Chem. B* **110**, 1807–1813 (2006).
32. M. Fang, S. Baldelli, Surface-induced heterogeneity analysis of an alkanethiol monolayer on microcrystalline copper surface using sum frequency generation imaging microscopy. *J. Phys. Chem. C* **121**, 1591–1601 (2017).
33. M. Flörsheimer, C. Brillert, H. Fuchs, Chemical imaging of interfaces by sum frequency microscopy. *Langmuir* **15**, 5437–5439 (1999).
34. V. Raghunathan, Y. Han, O. Korth, N.-H. Ge, E. O. Potma, Rapid vibrational imaging with sum frequency generation microscopy. *Opt. Lett.* **36**, 3891–3893 (2011).
35. Y. Fu, H. Wang, R. Shi, J. X. Cheng, Second harmonic and sum frequency generation imaging of fibrous astroglial filaments in ex vivo spinal tissues. *Biophys. J.* **92**, 3251–3259 (2007).
36. Y. Han *et al.*, Mapping molecular orientation with phase sensitive vibrationally resonant sum-frequency generation microscopy. *J. Phys. Chem. B* **117**, 6149–6156 (2013).
37. D. M. P. Hoffmann, K. Kuhnke, K. Kern, Sum-frequency generation microscope for opaque and reflecting samples. *Rev. Sci. Instrum.* **73**, 3221 (2002).
38. A. Tuladhar, S. Dewan, J. D. Kubicki, E. Borguet, Spectroscopy and ultrafast vibrational dynamics of strongly hydrogen bonded OH species at the α-Al2O3(112-0)/H2O interface. *J. Phys. Chem. C* **120**, 16153–16161 (2016).
39. J. A. McGuire, Y. R. Shen, Ultrafast vibrational dynamics at water interfaces. *Science* **313**, 1945–1948 (2006).

CHEMISTRY

40. S. Nihonyanagi, S. Yamaguchi, T. Tahara, Ultrafast dynamics at water interfaces studied by vibrational sum frequency generation spectroscopy. *Chem. Rev.* **117**, 10665–10693 (2017).

41. R. A. Livingstone, Y. Nagata, M. Bonn, E. H. G. Backus, Two types of water at the water-surfactant interface revealed by time-resolved vibrational spectroscopy. *J. Am. Chem. Soc.* **137**, 14912–14919 (2015).

42. Z. Zhang, L. Piatkowski, H. J. Bakker, M. Bonn, Ultrafast vibrational energy transfer at the water/air interface revealed by two-dimensional surface vibrational spectroscopy. *Nat. Chem.* **3**, 888–893 (2011).

43. W. Xiong, J. E. Laaser, R. D. Mehlenbacher, M. T. Zanni, Adding a dimension to the infrared spectra of interfaces using heterodyne detected 2D sum-frequency generation (HD 2D SFG) spectroscopy. *Proc. Natl. Acad. Sci. U.S.A.* **108**, 20902–20907 (2011).

44. M. Bonn et al., Structural inhomogeneity of interfacial water at lipid monolayers revealed by surface-specific vibrational pump-probe spectroscopy. *J. Am. Chem. Soc.* **132**, 14971–14978 (2010).

45. S. Woutersen, H. J. Bakker, Resonant intermolecular transfer of vibrational energy in liquid water. *Nature* **402**, 507–509 (1999).

46. R. L. A. Timmer, H. J. Bakker, Vibrational Förster transfer in ice Ih. *J. Phys. Chem. A* **114**, 4148–4155 (2010).

47. H. Wang, T. Gao, W. Xiong, Self-phase-stabilized heterodyne vibrational sum frequency generation microscopy. *ACS Photonics* **4**, 1839–1845 (2017).

48. S. Nihonyanagi, J. A. Mondal, S. Yamaguchi, T. Tahara, Structure and dynamics of interfacial water studied by heterodyne-detected vibrational sum-frequency generation. *Annu. Rev. Phys. Chem.* **64**, 579–603 (2013).

49. Y. R. Shen, Phase-sensitive sum-frequency spectroscopy. *Annu. Rev. Phys. Chem.* **64**, 129–150 (2013).

50. H.-F. Wang, L. Velarde, W. Gan, L. Fu, Quantitative sum-frequency generation vibrational spectroscopy of molecular surfaces and interfaces: Lineshape, polarization, and orientation. *Annu. Rev. Phys. Chem.* **66**, 189–216 (2015).

51. H. F. Wang, W. Gan, R. Lu, Y. Rao, B. H. Wu, Quantitative spectral and orientational analysis in surface sum frequency generation vibrational spectroscopy (SFG-VS). *Int. Rev. Phys. Chem.* **24**, 191–256 (2005).

52. S. T. van der Post et al., Strong frequency dependence of vibrational relaxation in bulk and surface water reveals sub-picosecond structural heterogeneity. *Nat. Commun.* **6**, 8384 (2015).

53. W. Saenger et al., Structures of the common cyclodextrins and their larger analogues - beyond the doughnut. *Chem. Rev.* **98**, 1787–1802 (1998).

54. I. V. Stiopkin et al., Hydrogen bonding at the water surface revealed by isotopic dilution spectroscopy. *Nature* **474**, 192–195 (2011).

55. C. P. Lawrence, J. L. Skinner, Vibrational spectroscopy of HOD in liquid D2O. III. Spectral diffusion, and hydrogen-bonding and rotational dynamics. *J. Chem. Phys.* **118**, 264–272 (2003).

56. A. Staib, J. T. Hynes, Vibrational predissociation in hydrogen-bonded OH...O complexes via OH stretch-OO stretch energy transfer. *Chem. Phys. Lett.* **204**, 197–205 (1993).

57. C. J. Fecko, J. D. Eaves, J. J. Loparo, A. Tokmakoff, P. L. Geissler, Ultrafast hydrogen-bond dynamics in the infrared spectroscopy of water. *Science* **301**, 1698–1702 (2003).

58. O. O. Sofronov, H. J. Bakker, Vibrational relaxation dynamics of the core and outer part of proton-hydration clusters. *J. Phys. Chem. B* **123**, 6222–6228 (2019).

59. L. Piatkowski, K. B. Eisenthal, H. J. Bakker, Ultrafast intermolecular energy transfer in heavy water. *Phys. Chem. Chem. Phys.* **11**, 9033–9038 (2009).

60. J. D. Cyran, E. H. G. Backus, Y. Nagata, M. Bonn, Structure from dynamics: Vibrational dynamics of interfacial water as a probe of aqueous heterogeneity. *J. Phys. Chem. B* **122**, 3667–3679 (2018).

61. E. T. J. Nibbering, T. Elsaesser, Ultrafast vibrational dynamics of hydrogen bonds in the condensed phase. *Chem. Rev.* **104**, 1887–1914 (2004).

62. S. J. Slater, C. Ho, F. J. Taddeo, M. B. Kelly, C. D. Stubbs, Contribution of hydrogen bonding to lipid-lipid interactions in membranes and the role of lipid order: Effects of cholesterol, increased phospholipid unsaturation, and ethanol. *Biochemistry* **32**, 3714–3721 (1993).

63. N. P. Stone, G. Demo, E. Agnello, B. A. Kelch, Principles for enhancing virus capsid capacity and stability from a thermophilic virus capsid structure. *Nat. Commun.* **10**, 4471 (2019).

64. A. J. Olson, Y. H. E. Hu, E. Keinan, Chemical mimicry of viral capsid self-assembly. *Proc. Natl. Acad. Sci. U.S.A.* **104**, 20731–20736 (2007).

65. R. Pandey et al., Ice-nucleating bacteria control the order and dynamics of interfacial water. *Sci. Adv.* **2**, e1501630 (2016).

66. X. Chen et al., Locking covalent organic frameworks with hydrogen bonds: General and remarkable effects on crystalline structure, physical properties, and photochemical activity. *J. Am. Chem. Soc.* **137**, 3241–3247 (2015).

67. T. Tsuzuki, M. Kabumoto, H. Arakawa, M. Ikeda, The effect of carbohydrate structures on the hydrogelation ability and morphology of self-assembled structures of peptide-carbohydrate conjugates in water. *Org. Biomol. Chem.* **15**, 4595–4600 (2017).

68. P. D. C. Dietzel, R. E. Johnsen, R. Blom, H. Fjellvåg, Structural changes and coordinatively unsaturated metal atoms on dehydration of honeycomb analogous microporous metal-organic frameworks. *Chemistry* **14**, 2389–2397 (2008).

69. K. Inoue, S. Nihonyanagi, P. C. Singh, S. Yamaguchi, T. Tahara, 2D heterodyne-detected sum frequency generation study on the ultrafast vibrational dynamics of H2O and HOD water at charged interfaces. *J. Chem. Phys.* **142**, 212431 (2015).

70. J. Bredenbeck, A. Ghosh, H. K. Nienhuys, M. Bonn, Interface-specific ultrafast two-dimensional vibrational spectroscopy. *Acc. Chem. Res.* **42**, 1332–1342 (2009).

71. H. Vanselous, A. M. Stingel, P. B. Petersen, Interferometric 2D sum frequency generation spectroscopy reveals structural heterogeneity of catalytic monolayers on transparent materials. *J. Phys. Chem. Lett.* **8**, 825–830 (2017).

72. J. Wang et al., Short-range catalyst-surface interactions revealed by heterodyne two-dimensional sum frequency generation spectroscopy. *J. Phys. Chem. Lett.* **6**, 4204–4209 (2015).

73. W. R. Silva, C. T. Graefe, R. R. Frontiera, Toward label-free super-resolution microscopy. *ACS Photonics* **3**, 79–86 (2016).

74. S. W. Hell, J. Wichmann, Breaking the diffraction resolution limit by stimulated emission: Stimulated-emission-depletion fluorescence microscopy. *Opt. Lett.* **19**, 780–782 (1994).

75. B. Harke et al., Resolution scaling in STED microscopy. *Opt. Express* **16**, 4154–4162 (2008).

76. N. A. Moringo, H. Shen, L. D. C. Bishop, W. Wang, C. F. Landes, Enhancing analytical separations using super-resolution microscopy. *Annu. Rev. Phys. Chem.* **69**, 353–375 (2018).

77. B. M. Luther, K. M. Tracy, M. Gerrity, S. Brown, A. T. Krummel, 2D IR spectroscopy at 100 kHz utilizing a Mid-IR OPCPA laser source. *Opt. Express* **24**, 4117–4127 (2016).

78. R. Gutzler et al., Halogen bonds as stabilizing interactions in a chiral self-assembled molecular monolayer. *Chem. Commun. (Camb.)* **47**, 9453–9455 (2011).

79. M. Liu, L. Zhang, T. Wang, Supramolecular chirality in self-Assembled systems. *Chem. Rev.* **115**, 7304–7397 (2015).